The International Journal of Advanced Manufacturing Technology (2025) 139:4125–4139
https://doi.org/10.1007/s00170-025-16116-3

ORIGINAL ARTICLE

Thermal history and microstructural evolution in MIG-Wire Arc Additive Manufacturing of low carbon steel: influence of key process parameters

Francesco Lambiase[1] · **Phanidra Babu Yanala**[1] · **Francesco Pace**[1] · **Elena Andreucci**[1] · **Alfonso Paoletti**[1]

Received: 22 April 2025 / Accepted: 9 July 2025 / Published online: 26 July 2025
© The Author(s) 2025

Abstract
This study investigates the influence of wire feed rate (WFR) and travel speed (TS) on Wire Arc Additive Manufacturing (WAAM) through a comprehensive experimental approach. Using an instrumented CNC machine with integrated voltage and current sensors, along with thermal IR imaging, we monitored process parameters and temperature evolution during multi-layer depositions. The experimental results revealed significant correlations between processing parameters and deposited bead geometry, microstructure, and mechanical properties. At lower travel speeds (250 mm/min), cooling rates remained relatively constant (~ 27 °C/s) across subsequent depositions, while higher travel speeds (1000 mm/min) produced significantly higher cooling rates (up to 115 °C/s) that varied with distance from the base plate. These variations in cooling rates directly influenced microstructural development, with higher travel speeds producing finer grain structures and increased microhardness (up to 283 HV compared to 237 HV at lower speeds). The study establishes predictive models for bead geometry based on mass conservation principles and identifies critical factors affecting microstructural evolution throughout the build height. These findings provide valuable insights for optimizing WAAM processing parameters to achieve desired geometrical accuracy and mechanical properties in additively manufactured components.

Keywords Additive Manufacturing · Wire Arc Additive Manufacturing · WAAM · Characterization · Signal processing

Abbreviations

CS	Cross section [mm^2]
Ts	Travel speed [mm/min]
WFS	Wire feed speed [mm/min]
WS	Wire section [mm^2]
$\overline{h}_d$	Average deposition height [mm]
$\overline{w}_d$	Theorical average width [mm]
AR	Aspect ratio [%]

1 Introduction

Additive manufacturing (AM) is transforming traditional manufacturing paradigms by enabling the creation of complex, customized components that would be impractical with conventional methods [1]. Among various AM techniques, Wire Arc Additive Manufacturing (WAAM) has emerged as a promising technology for producing large-scale metal components with high deposition rates. WAAM utilizes an electric arc to melt wire feedstock, depositing material layer by layer to build three-dimensional structures. This process offers significant advantages for industries requiring large, high-strength components, including aerospace [2], marine, and construction sectors.

WAAM provides several key benefits compared to other metal AM processes: (1) high material deposition rates, significantly reducing production times [3]; (2) cost-effectiveness, as wire feedstock is less expensive and generates less waste than powder-based alternatives; (3) versatility in processing various metals including titanium [4, 5], aluminum [6, 7], stainless steel [8, 9], and Inconel [10, 11]; and (4) capability for repair and refurbishment of existing components. These advantages make WAAM particularly valuable for low-volume, custom manufacturing applications that require rapid turnaround times. Despite these advantages, several challenges limit the widespread industrial adoption of WAAM. Residual stresses and distortion frequently occur due to high thermal

✉ Francesco Lambiase
francesco.lambiase@univaq.it

[1] Dept. of Industrial and Information Engineering and Economics, University of L'Aquila, Zona Industriale Di Pile, Via G. Gronchi 18, L'Aquila, Italy 67100

gradients and rapid cooling rates inherent to the process, leading to dimensional instability [12, 13]. Microstructural and mechanical heterogeneity often results from the layer-by-layer deposition process, introducing variations in material properties throughout the part [14]. Wang et al. [15] demonstrated that Ti-6Al-4V WAAM components exhibited anisotropic microstructures with large equiaxed grains near the substrate and finer structures in the top layers, resulting in position-dependent mechanical properties. Similar heterogeneity was observed by Wang et al. [16] in AZ31 magnesium alloy and [17] AA5356 WAAM components, where repeated heating cycles created non-uniform properties affecting grain size, microhardness, and tensile characteristics.

Compared to powder bed fusion processes [18], WAAM faces greater challenges in producing complex geometries with high precision. Process parameter optimization is therefore crucial for achieving desired geometrical accuracy and material quality. Vora et al. [19] developed regression models to correlate process parameters with build quality, while Han et al. [20] investigated the effects of welding parameters on the fabrication of complex propeller-shaped components. Proper selection of process parameters, scan strategies, and post-processing techniques can mitigate these challenges [21]. Process monitoring remains essential for ensuring quality and stability during WAAM. Rahman et al. [22] demonstrated the effectiveness of acoustic emission monitoring for multilayer deposition processes, while Franke et al. [23] implemented real-time image analysis using neural networks to monitor wire segmentation and spatter formation. These approaches enable closed-loop control for complex deposition paths and improved process stability. Despite recent advances, several fundamental questions regarding WAAM process optimization remain unanswered:

- How do wire feed rate and travel speed affect the geometry of deposited beads during multilayer deposition?
- Can theoretical models based on mass conservation accurately predict bead geometry under various processing conditions?
- How do process parameters influence electrical characteristics (current, voltage) and thermal history during deposition?
- What are the relationships between thermal history, microstructure evolution, and mechanical properties in multilayer WAAM components?

This study addresses these questions through a systematic experimental investigation that varies travel speed and wire feed rate during WAAM. We employ in-process monitoring of electrical parameters and temperature evolution via IR thermography, coupled with post-process analysis of geometry, microstructure, and microhardness. This comprehensive approach provides valuable insights into the complex relationships between process parameters and the resulting material characteristics, enabling more effective optimization of WAAM for industrial applications.

2 Materials and methods

2.1 Experimental setup and materials

Deposition experiments were conducted using a prototype CNC machine equipped with a MIG WELD 303 C torch. Substrate plates (100 mm × 30 mm × 3.3 mm) were securely clamped to the CNC machine table using a customized fixture. Argon shielding gas was supplied at a flow rate of 10 L/min. The deposited material was a low-carbon steel wire with a diameter of 1.0 mm. The chemical compositions of both the substrate plate and the wire feedstock are presented in Table 1.

2.2 Process monitoring

Real-time measurements of voltage and current were performed during deposition using an LV25-P voltage transducer and an LF306-S current transducer. Signals were recorded via a National Instruments USB6009 I/O board at a sampling rate of 1.0 kHz. Thermal history was monitored using a FLIR A615 infrared camera with a frame rate of 200 Hz and a resolution of 640 × 480 pixels, capable of measuring temperatures up to approximately 2000 °C. The FLIR ResearchIR software was used for thermal data acquisition and analysis. This setup allowed for detailed characterization of temperature variations at specific locations during deposition, providing insights into the relationships between process parameters and thermal history. Figure 1 shows the schematic of the integration experimental setup.

2.3 Experimental design

Preliminary experiments were conducted to identify stable processing conditions with consistent arc stability and material deposition. Based on these tests, a constant voltage of 26 V was selected. Multilayer depositions consisted

Table 1 Chemical composition of the materials involved

Element	C	Cu	Mn	Ni	Ti	Zn
Wire [wt.%]	1.009	5.469	1.321	0.096	0.039	0.016
Substrate [wt.%]	1.317	0.591	0.427	0.294	0.196	0.195

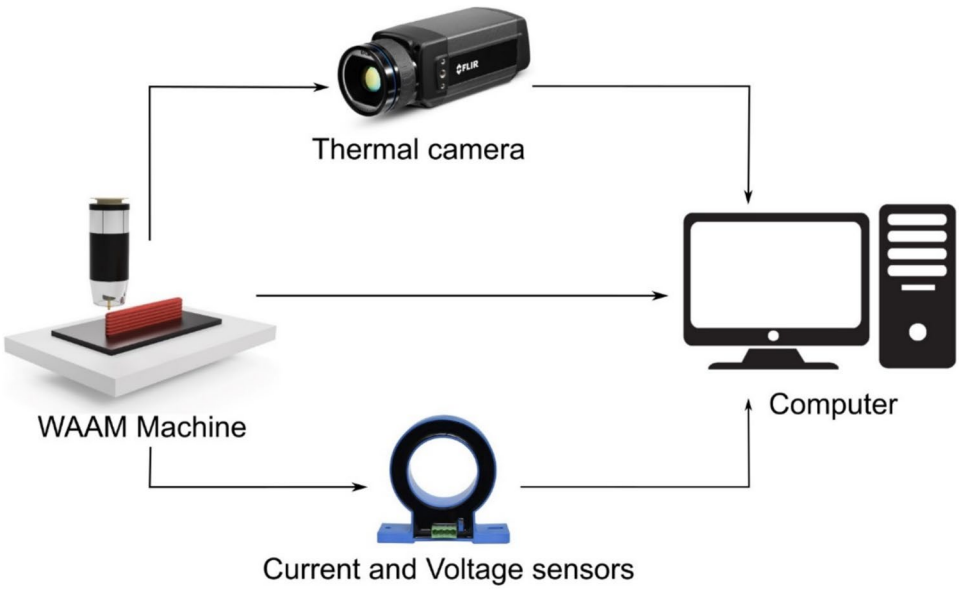


Fig. 1 Experimental setup for WAAM deposition with integrated monitoring systems

Table 2 Process parameters for experimental investigation

Travel speed, TS [mm/min]	Wire feed speed, WFS [mm/min]
250	3900
500	5800
750	
1000	

of 10 layers with forced air cooling between consecutive depositions, with the waiting time of 150 s chosen to restore the substrate temperature to 50 °C. Such value, which is close to the ambient temperature, is small enough to achieve consistent subsequent depositions (in terms of initial substrate temperature). Multilayer depositions consisted of 10 layers with forced air cooling between consecutive depositions to restore an initial temperature below 50 °C, requiring a cooling time of 150 s between consecutive layers. Alternating deposition directions were employed to prevent uneven build-up [24, 25]. The experimental plan employed two principal variables: travel speed (TS) and wire feed speed (WFS). Travel speed was varied at four levels (250, 500, 750, and 1000 mm/min), while wire feed speed was set at two levels (3900 and 5800 mm/min), resulting in eight experimental conditions as summarized in Table 2. The maximum travel speed was selected based on the CNC machine capability, while the wire feed rate was selected based on preliminary tests. Lower values of wire feed rates did not ensure consistent depositions (especially under high values of the travel speed); on the other hand, higher values of the wire feed rates (> 5800 mm/min) also led to lack of adhesion with the substrate (especially under high travel speed).

2.4 Characterization methods

Microstructural analysis was performed on cross-sectioned samples extracted from the midpoint of each deposit. Samples were mounted in CEM1000 Blue epoxy resin, ground with abrasive papers up to 2500 grit, and polished using CT Dia Twin Poly (6 mm) with 0.2 µm alkaline fumed silica suspension. Chemical etching was performed using Nital etchant (4% HNO_3 in ethanol) for 10 s, followed by rinsing in distilled water. Microstructural examination was conducted using a Leica DM5000 optical microscope.

Microhardness testing was performed using a Mitutoyo HM-112 microhardness tester according to ASTM E140 standards. Measurements were taken with an indentation load of 1 N and a dwell time of 15 s at specified locations along the build height to characterize hardness variations.

Geometrical measurements of the deposited beads were obtained from cross-sectional images to determine key parameters including average layer height, bead width, and cross-sectional area. These measurements enabled quantitative assessment of the relationships between process parameters and deposit geometry.

3 Results

3.1 Current, voltage, and power

Figure 2a presents the current and voltage measurements during the deposition of the first layer. The voltage signal remained relatively constant at the set value of 26 V, while the current exhibited periodic fluctuations characterized by localized drops. These fluctuations reflect variations in the

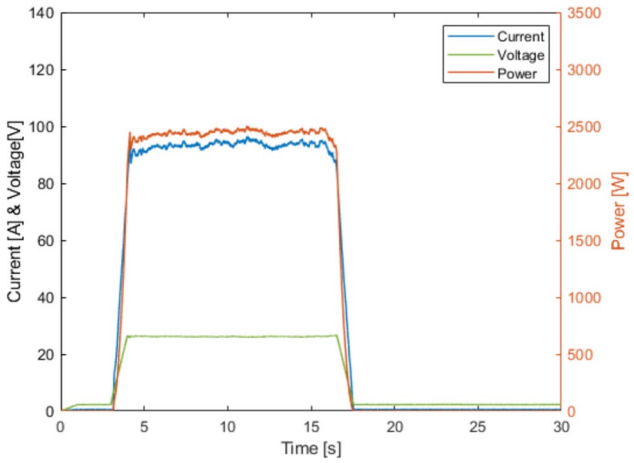


Fig. 2 Current and voltage signals and power signals measured during first layer deposition

arc stability and deposition regularity during the process. Figure 2b shows the corresponding power signal, calculated as the product of current and voltage, which follows the same pattern as the current due to the relatively constant voltage.

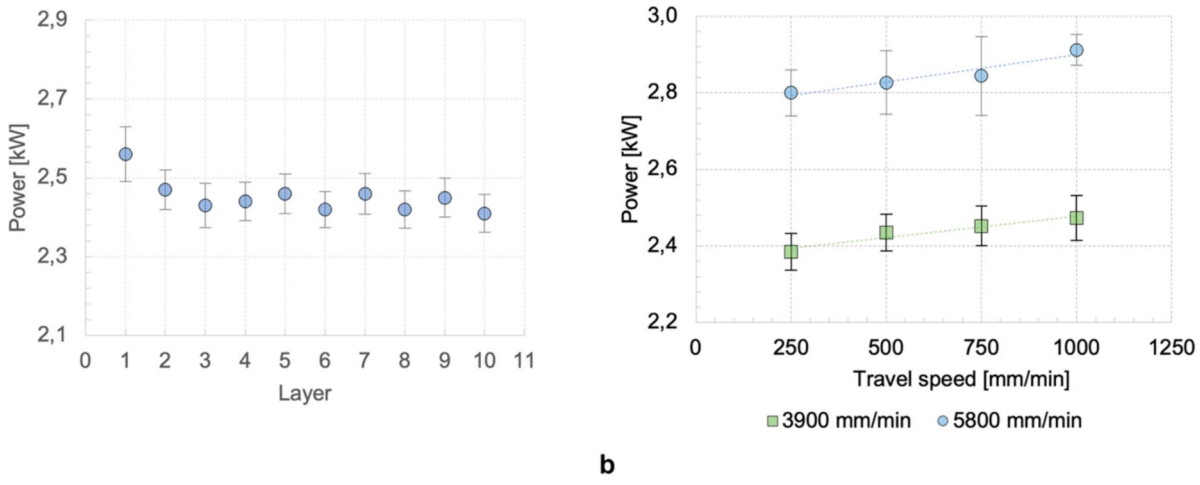
The electrical characteristics evolved during multilayer deposition, with the average power decreasing with increasing build height. Figure 3 illustrates this trend for the condition using 500 mm/min travel speed and 3900 mm/min wire feed rate. During the first layer deposition, the average power was 2.53 kW, which decreased to 2.40 kW by the third layer, representing a reduction of 5.1%. This power reduction is attributed to the changing thermal and electrical conditions between the substrate and previously deposited layers. The initial layer is deposited onto the substrate plate with relatively high electrical conductivity, while subsequent layers are deposited onto narrower areas with higher electrical resistance, resulting in reduced current flow.

3.2 Geometrical characteristics of deposited beads

Ten-layer wall structures were successfully produced under all experimental conditions. Figure 4 shows the macroscopic appearance and cross-sectional images of the deposited samples. Clear differences in bead geometry were observed as a function of process parameters. Lower travel speeds produced wider and taller beads due to increased material deposition per unit length, while higher travel speeds resulted in narrower and shorter beads. Similarly, higher wire feed rates generated wider and taller beads compared to lower wire feed rates; these findings are consistent with those reported by Dinovitzer et al. [26]. Notably, deposits produced at higher wire feed rates and travel speeds exhibited greater geometrical irregularity; similarly, Vishwanatha et al. [27] reported that lower travel speeds improved the layer uniformity.

The average layer height was determined by dividing the total wall height by the number of deposited layers (10), as illustrated in Fig. 5. This approach provides a representative measure of the layer height while accounting for minor variations between individual layers.

Figure 6a shows the average layer height as a function of travel speed for both wire feed rates. The height decreased logarithmically with increasing travel speed, reflecting the reduced material deposition per unit length at higher travel speeds. For a given travel speed, higher wire feed rates produced taller layers due to increased material input. Similar trends were observed for the cross-sectional area (Fig. 6b) and average bead width (Fig. 6c).



a b

Fig. 3 **a** Variation of average power measured during multilayer deposition with travel speed of 500 mm/min and wire feed rate of 3900 mm/min. **b** Average power measured in different samples during the process

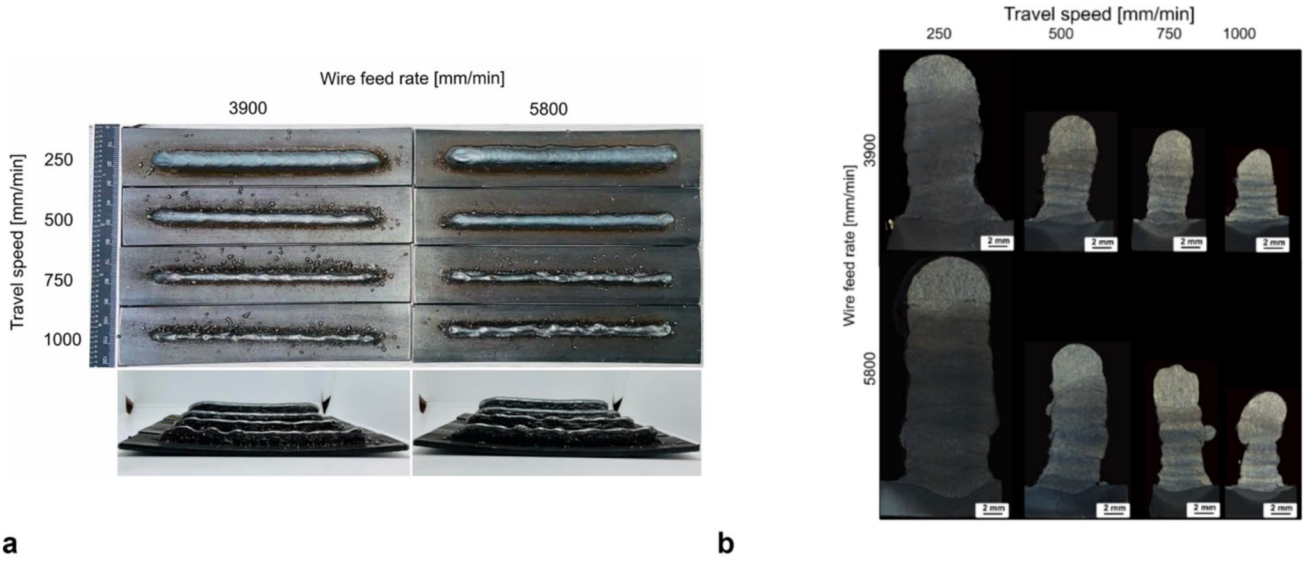


Fig. 4 **a** Top and side views of experimental samples after deposition and **b** cross-sectional images of samples produced under different processing conditions

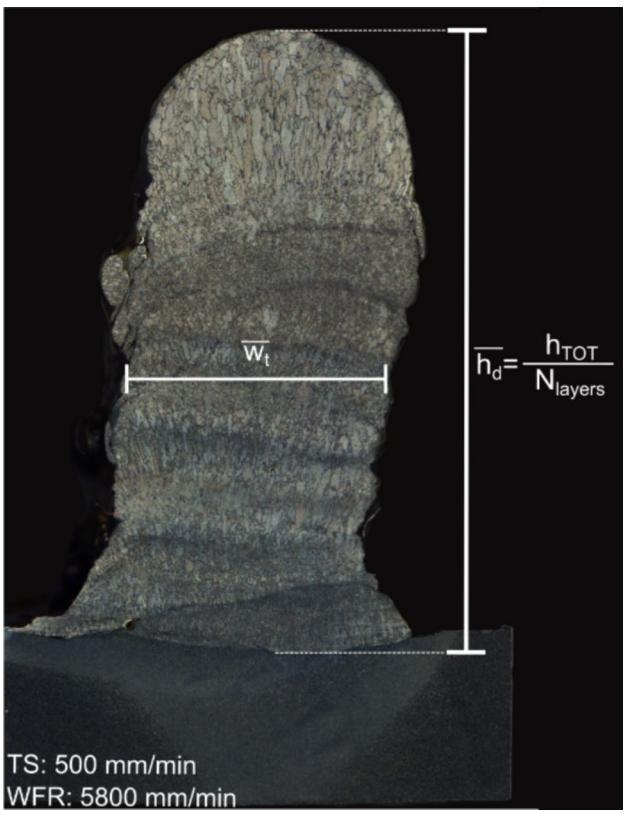


Fig. 5 Measurement scheme for determining average deposition height ($\bar{h}_e$) and average experimental width ($\bar{w}_e$)

The aspect ratio (height-to-width ratio) ranged from 23 to 31% across all experimental conditions (Fig. 6d). This relatively narrow range suggests a consistent relationship between height and width despite variations in absolute dimensions, indicating predictable bead geometry formation mechanisms.

A theoretical model based on mass conservation was developed to predict the cross-sectional area of deposited beads:

$$CS = \frac{1}{T_s} \times WFS \times WS \tag{1}$$

where CS is the cross-sectional area, TS is the travel speed, WFS is the wire feed speed, and WS is the wire cross-sectional area. The theoretical width ($\bar{w}_t$) can then be calculated as:

$$\overline{w}_t = \frac{CS}{\overline{h}_d} \tag{2}$$

and the aspect ratio (AR) as:

$$AR = \frac{\overline{h}_d}{\overline{w}_t} \tag{3}$$

Figure 7 compares the experimental cross-sectional areas with predictions from the mass conservation model. Excellent agreement was observed across all process conditions, validating the model's accuracy for predicting bead geometry based on process parameters.

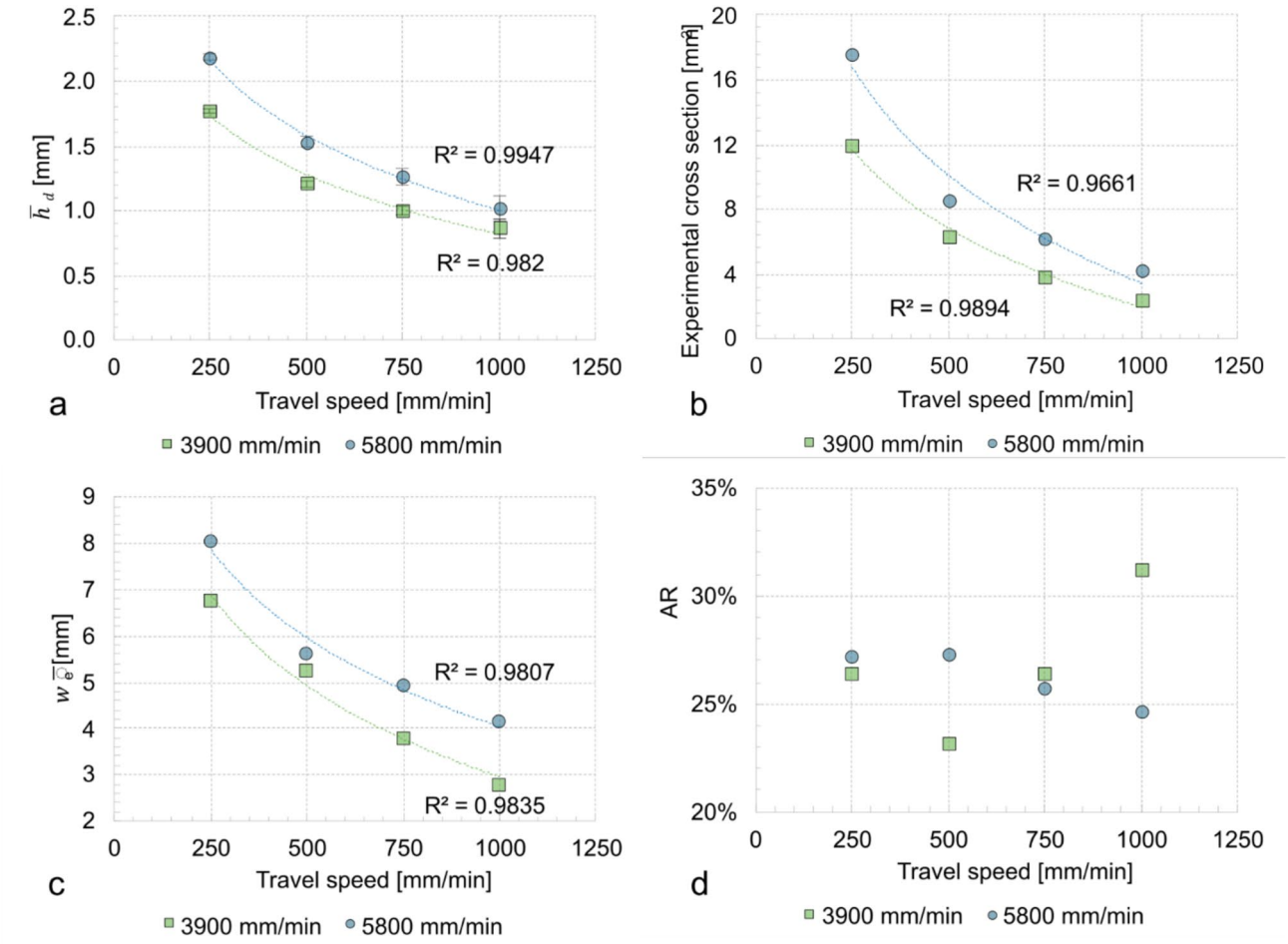


Fig. 6 Geometric characteristics of deposited beads: **a** average layer height, **b** cross-sectional area, **c** average width, and **d** aspect ratio, as functions of travel speed for different wire feed rates

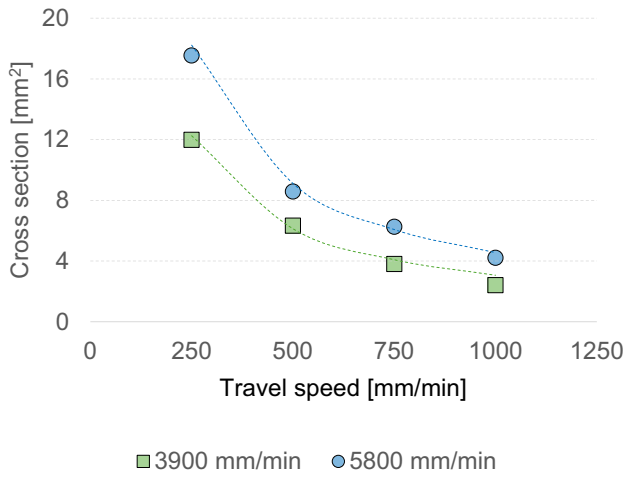


Fig. 7 Comparison of experimental measurements (markers) of cross-sectional area with model predictions (dotted lines) based on mass conservation

3.3 Thermal history and cooling rates

Infrared thermal imaging was used to monitor temperature evolution during multilayer deposition. An emissivity coefficient of 0.45 was employed based on previous studies [28]. Figure 8a shows a representative thermal image captured during the fifth layer deposition. A vertical line region of interest (ROI) was established at the center of the deposit to track temperature variations over time, with the maximum temperature along this line calculated for each frame (Fig. 8b).

The temperature–time profile exhibits two distinct peaks, as illustrated in Fig. 9. This pattern results from the relative positions of the IR camera, deposit, and MIG torch. The temporary temperature drop between peaks occurs when the torch momentarily obscures the upper portion of the ROI from the camera's view, creating an artifact in the temperature recording.

Figure 10 presents the temperature evolution during fifth layer deposition for all experimental conditions. Clear

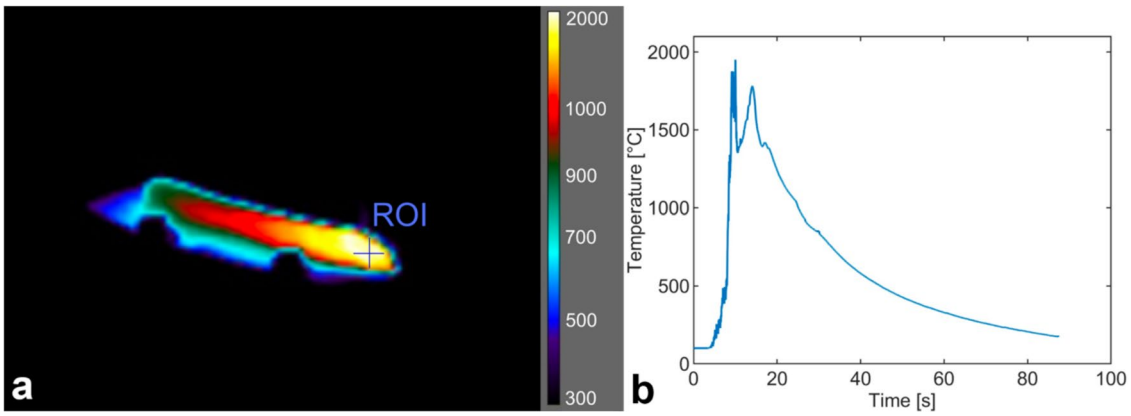


Fig. 8 **a** Infrared thermal image during fifth layer deposition and **b** corresponding temperature evolution at the central ROI

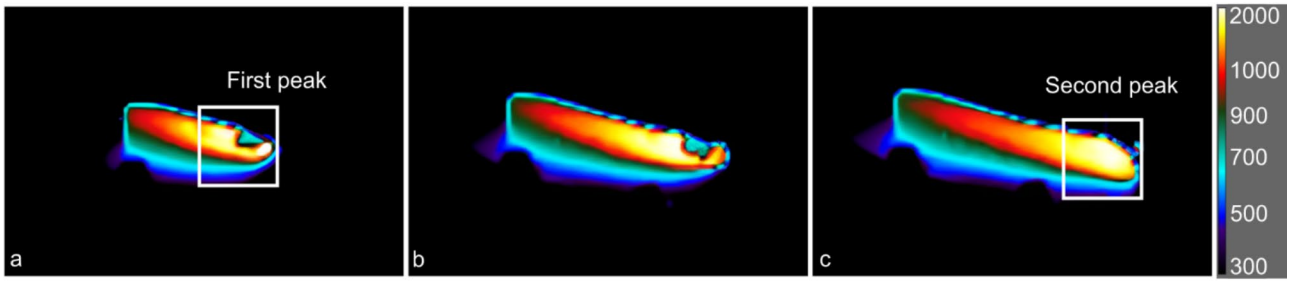


Fig. 9 Sequential thermal images showing the origin of double temperature peaks during deposition

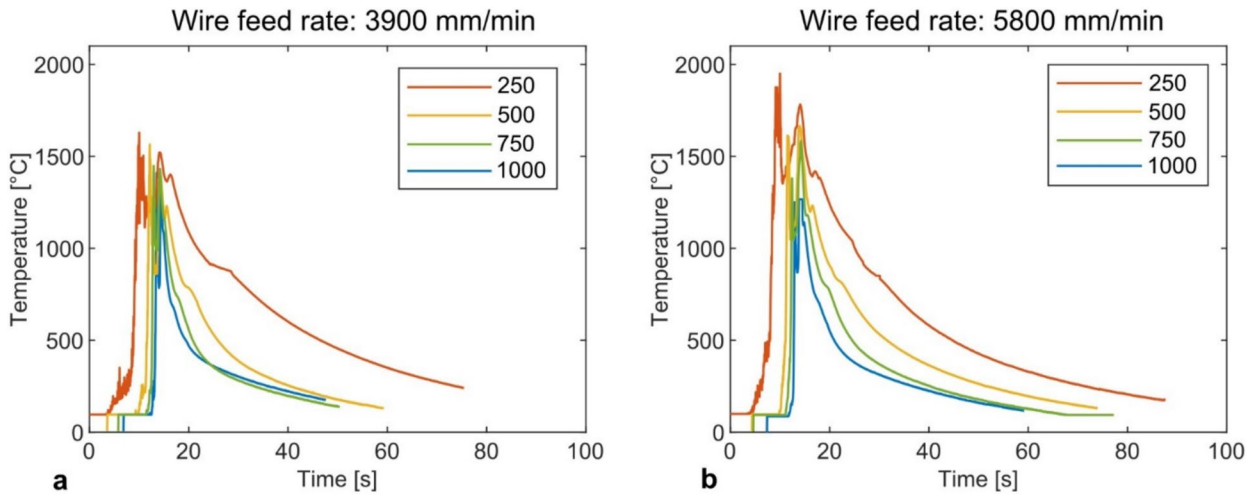


Fig. 10 Temperature distributions during deposition at different travel speeds with wire feed rates of **a** 3900 mm/min and **b** 5800 mm/min

differences in cooling rates were observed as functions of both travel speed and wire feed rate. Higher travel speeds resulted in faster cooling rates due to reduced heat input and material deposition per unit length. Conversely, higher wire feed rates produced slower cooling rates owing to increased thermal mass, which enhances heat retention in the deposited material.

To quantify these differences, cooling rates were calculated as the temperature change rate between the peak temperature (T_1) and 400 °C (T_2), as illustrated in Fig. 11.

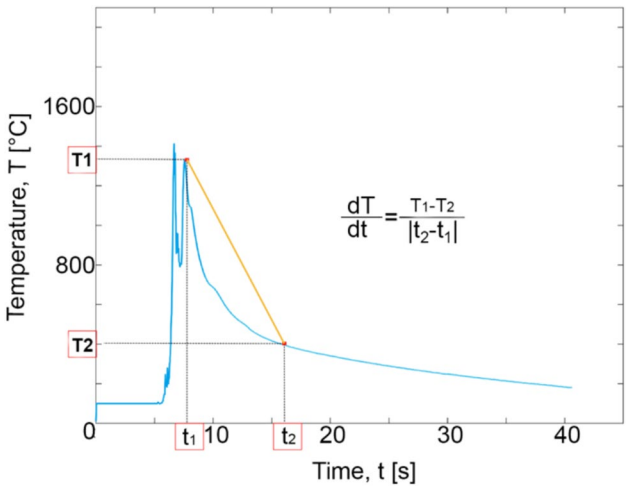


Fig. 11 Schematic representation of the cooling rate determination method

Figure 12 presents the layer-by-layer evolution of cooling rates for all experimental conditions. At the lowest travel speed (250 mm/min), cooling rates remained nearly constant across all layers for both wire feed rates. In contrast, at higher travel speeds (500–1000 mm/min), cooling rates varied with build height, generally increasing until the sixth layer before gradually decreasing. The sample produced with a 5800 mm/min wire feed rate and 1000 mm/min travel speed exhibited irregular cooling behavior after the fourth layer, likely due to the geometrical instability of the deposited bead.

Figure 13 summarizes the average cooling rates across all layers for each experimental condition. Samples produced with 5800 mm/min wire feed rate consistently exhibited lower cooling rates than those produced with 3900 mm/min, confirming the significant influence of thermal capacitance on cooling behavior. A notable interaction effect was observed between travel speed and wire feed rate. At low travel speed (250 mm/min), cooling rates were similar (~ 27 °C/s) regardless of wire feed rate. However, at high travel speed (1000 mm/min), samples produced with 3900 mm/min wire feed rate cooled significantly faster (85 °C/s) than those produced with 5800 mm/min (73 °C/s). Overall, increasing travel speed from 250 mm/min to 1000 mm/min increased the average cooling rate by approximately 315% for 3900 mm/min wire feed rate and 270% for 5800 mm/min wire feed rate.

3.4 Microstructural characteristics and mechanical properties

Microstructural analysis was performed at various locations along the build height, as indicated in Fig. 14a. Distinct microstructural variations were observed, like observations reported in [29, 30] between the substrate/heat-affected zone (Fig. 14d), middle region (Fig. 14c), and top layers (Fig. 14b). These variations reflect the different thermal histories experienced at each location during the multilayer deposition process.

The observed microstructures consisted predominantly of ferrite and pearlite phases. The distribution and morphology of these phases varied with location and processing conditions. In the middle region (Fig. 14c) and substrate–heat-affected zone (Fig. 14d), distinct pearlite colonies were observed within a ferritic matrix. This microstructure typically develops under relatively slow cooling conditions. In contrast, the top region (Fig. 14b) exhibited a finer microstructure with more evenly distributed pearlite, characteristic of more rapid cooling.

Figure 15 presents the average grain size measurements at different locations for all experimental conditions. A clear

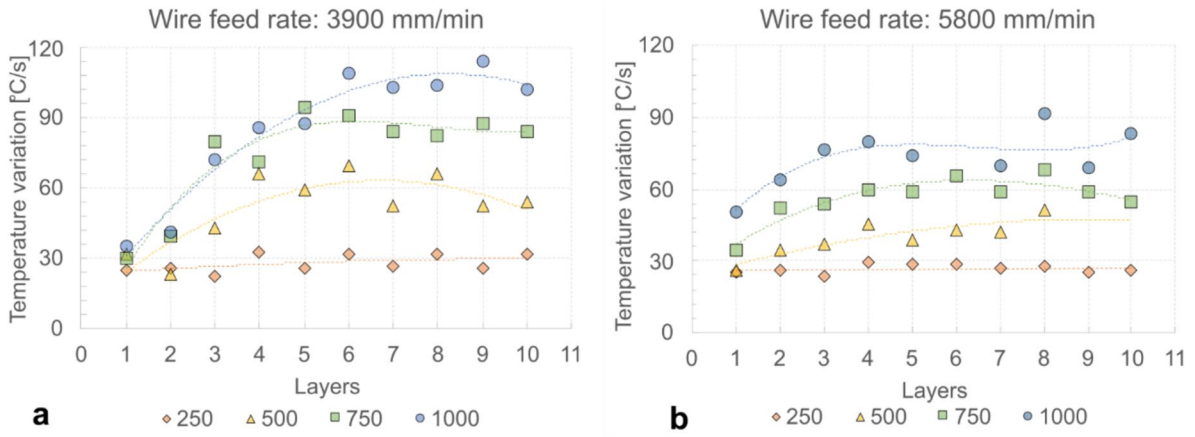


Fig. 12 Layer-by-layer cooling rates during multilayer deposition at different travel speeds with wire feed rates of **a** 3900 mm/min and **b** 5800 mm/min

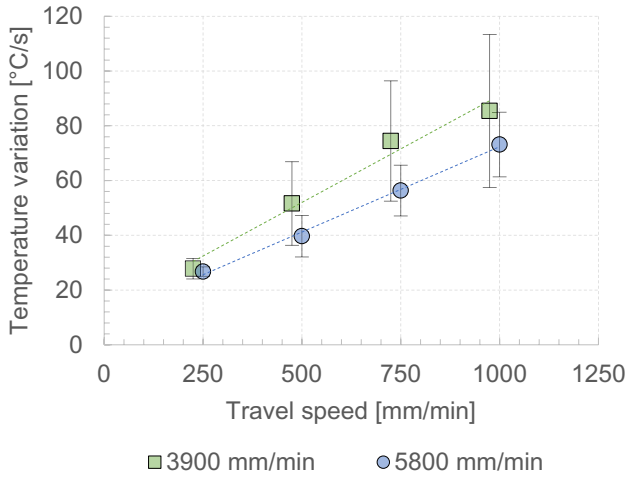


Fig. 13 Average of the temperature gradient at different wire feed rates

trend of decreasing grain size with increasing travel speed was observed across all samples. Additionally, samples produced with 3900 mm/min wire feed rate exhibited consistently finer grain structures (1–6 µm) compared to those produced with 5800 mm/min (1–8 µm), corresponding to the higher cooling rates experienced at the lower wire feed rate. For all conditions, grain size decreased from the bottom to the top of the sample, reflecting the evolution of thermal conditions and reduced reheating cycles in the upper layers.

The grain size measurement was performed using the Eq. 4 according to ASTM E112-13 (2021) [31].

$$Avggrainsize = \frac{Linelength}{Numberofgrains} \tag{4}$$

Figures 16 and 17 present detailed microstructural images at 1000× magnification for samples produced with wire feed rates of 3900 mm/min and 5800 mm/min, respectively. The microstructures evolved from predominantly equiaxed grains in the substrate/heat-affected zone to increasingly columnar grains with increasing build height. This transition reflects the directional heat flow and epitaxial grain growth characteristic of the WAAM process.

Microhardness measurements (Figs. 18 and 19) revealed significant variations in mechanical properties as functions of both process parameters and location within the build. In accordance with the Hall–Petch relationship [32], finer grain structures corresponded to higher hardness values.

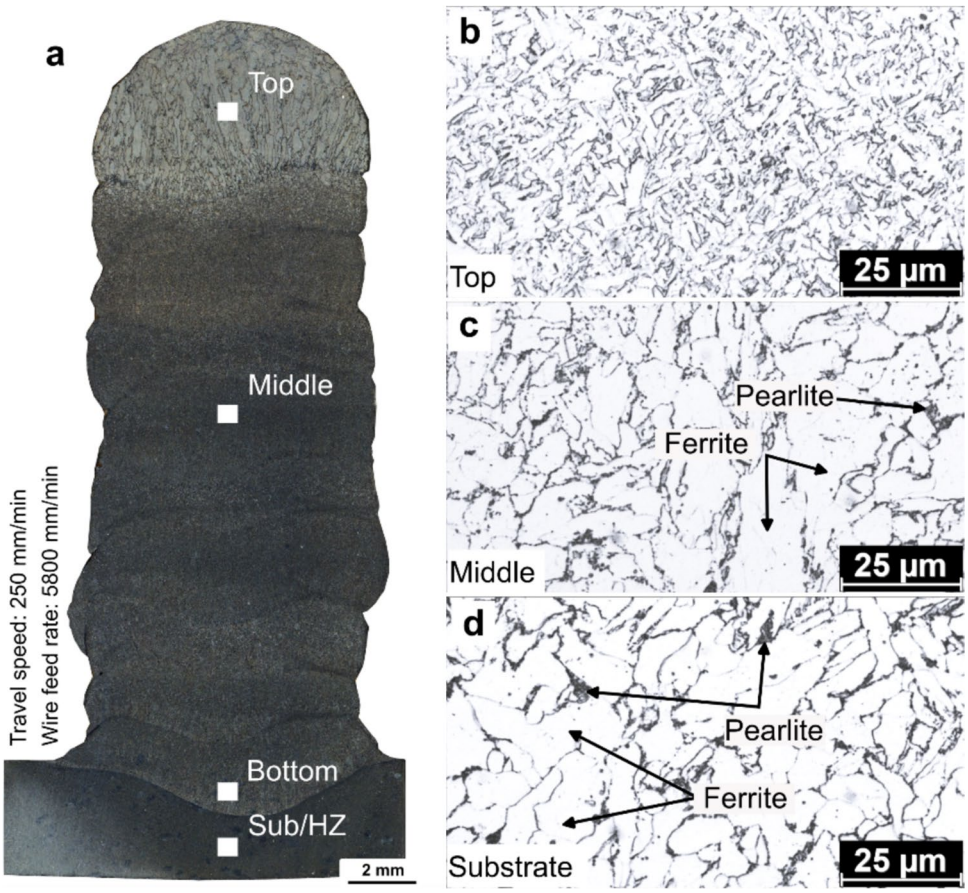


Fig. 14 **a** Measurement locations for microstructural analysis and representative microstructures at the **b** top, **c** middle, and **d** substrate/heat-affected zone regions

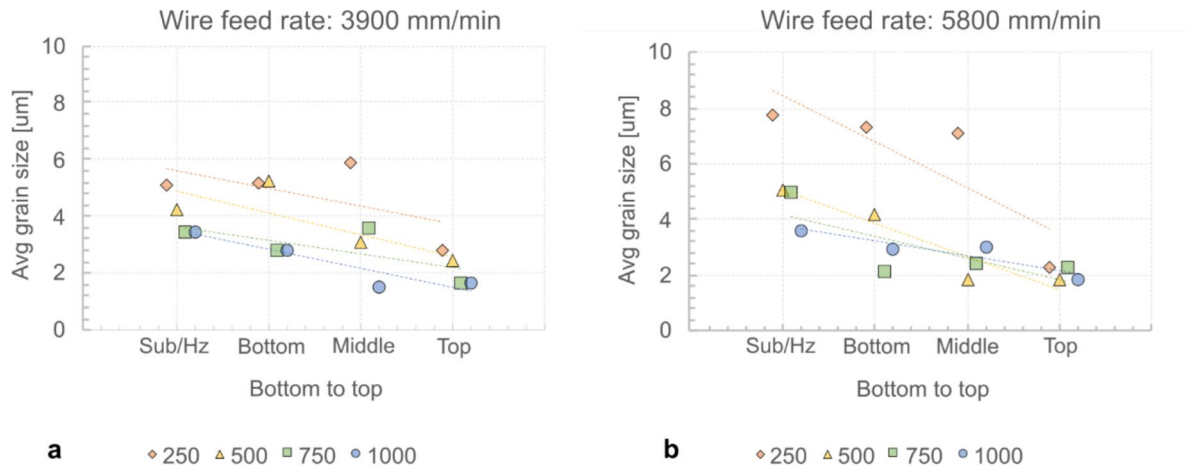


Fig. 15 Average grain size at different locations for samples produced with wire feed rates of **a** 3900 mm/min and **b** 5800 mm/min

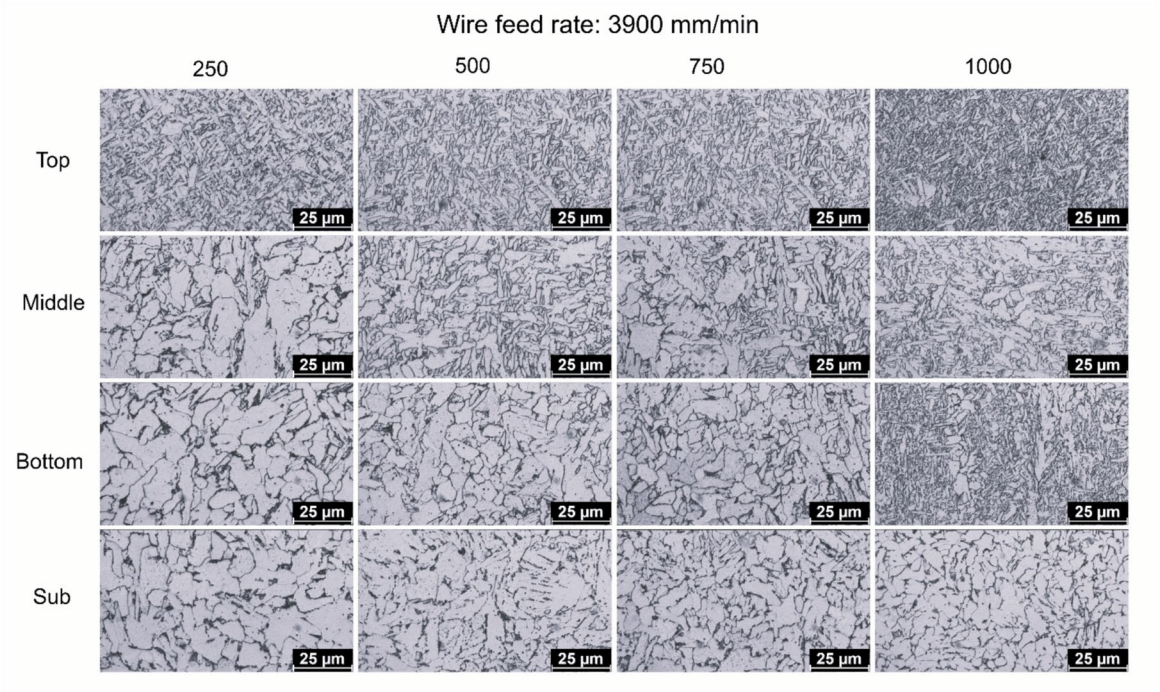


Fig. 16 Microstructure at various locations for samples produced with different travel speeds at 3900 mm/min wire feed rate

Consequently, samples produced at higher travel speeds exhibited greater hardness than those produced at lower travel speeds. Peak hardness was observed in the top layers of all samples due to the rapid cooling experienced by the final deposit and the absence of subsequent thermal cycles.

The microhardness distribution typically followed a characteristic pattern: lower values near the substrate, gradually increasing to a plateau in the middle region, followed by another increase toward the top layers. This "saddle-shaped" distribution reflects the combined effects of thermal cycling, microstructural evolution, and position-dependent cooling rates. As reported in the early article Lambiase et al. [33], initial layers undergo more thermal cycles compared to the middle and top layers. Average hardness values ranged from approximately 237 HV for samples produced at the lowest travel speed (250 mm/min) to 283 HV for those produced at the highest travel speed (1000 mm/min), demonstrating the significant influence of processing conditions on mechanical properties.

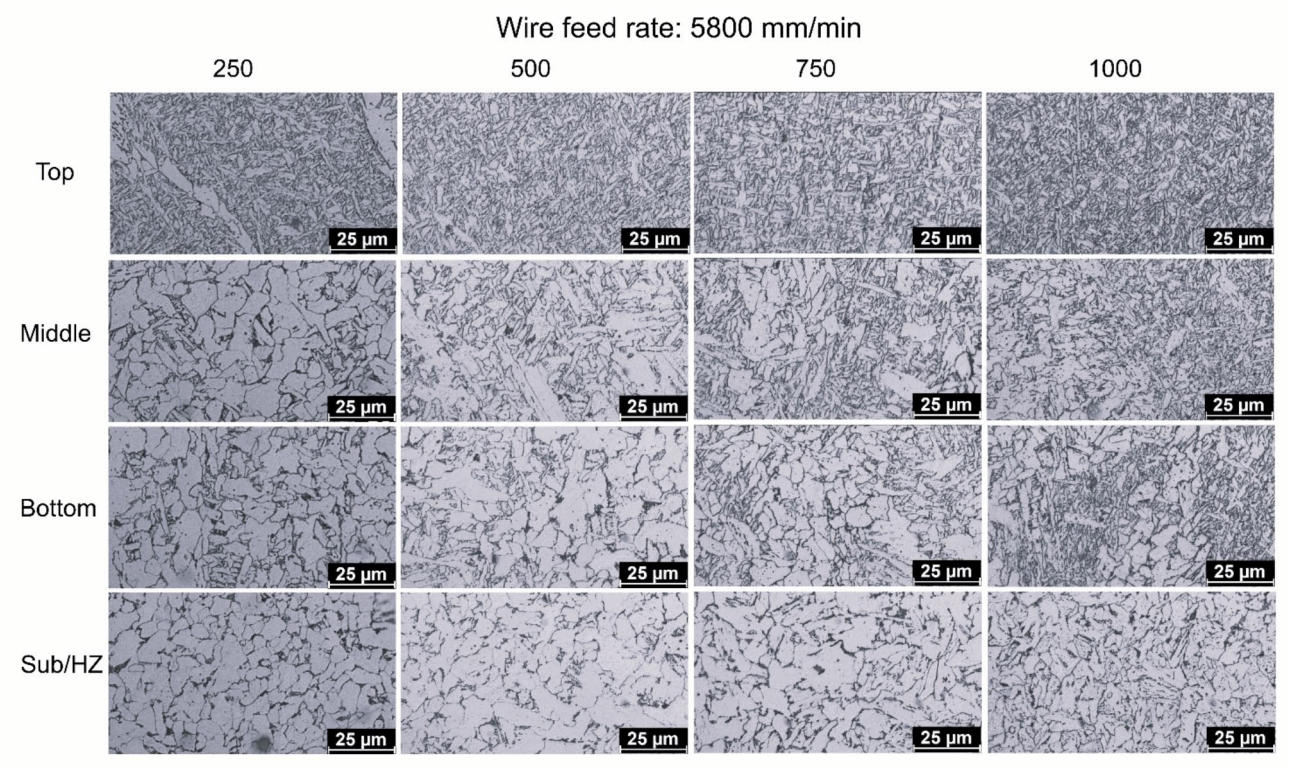


Fig. 17 Microstructure at various locations for samples produced with different travel speeds at 5800 mm/min wire feed rate

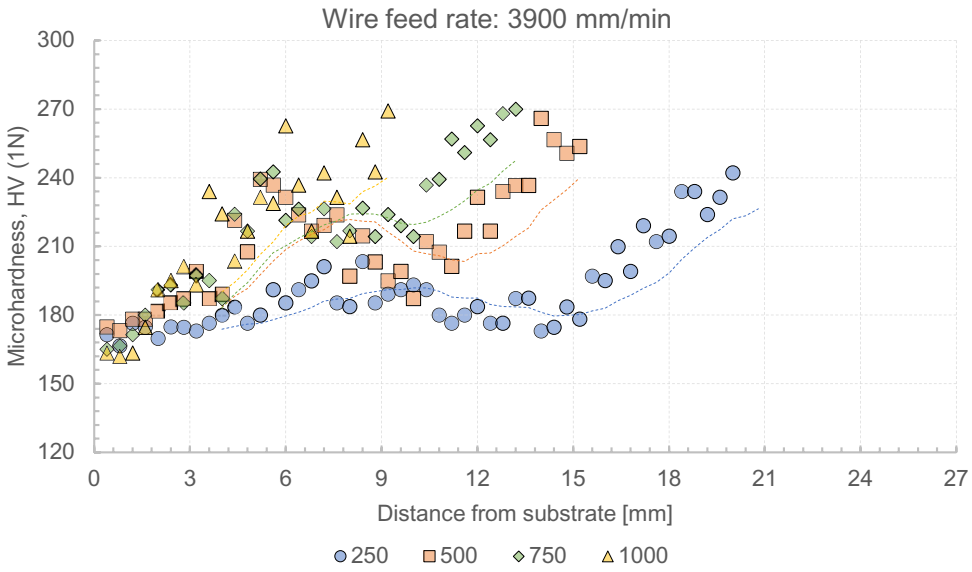


Fig. 18 Microhardness profiles for samples produced with different travel speeds at 3900 mm/min wire feed rate

4 Discussion

Wire Arc Additive Manufacturing (WAAM) addresses many limitations of other metal additive manufacturing processes, particularly regarding component size and production costs. While WAAM does not inherently provide the high geometric precision or surface quality achieved by powder-based processes, these limitations can be mitigated through post-processing operations such as machining. A more fundamental challenge lies in controlling the microstructural evolution during multilayer deposition, which significantly impacts mechanical properties. Unlike conventional heat treatments that can homogenize

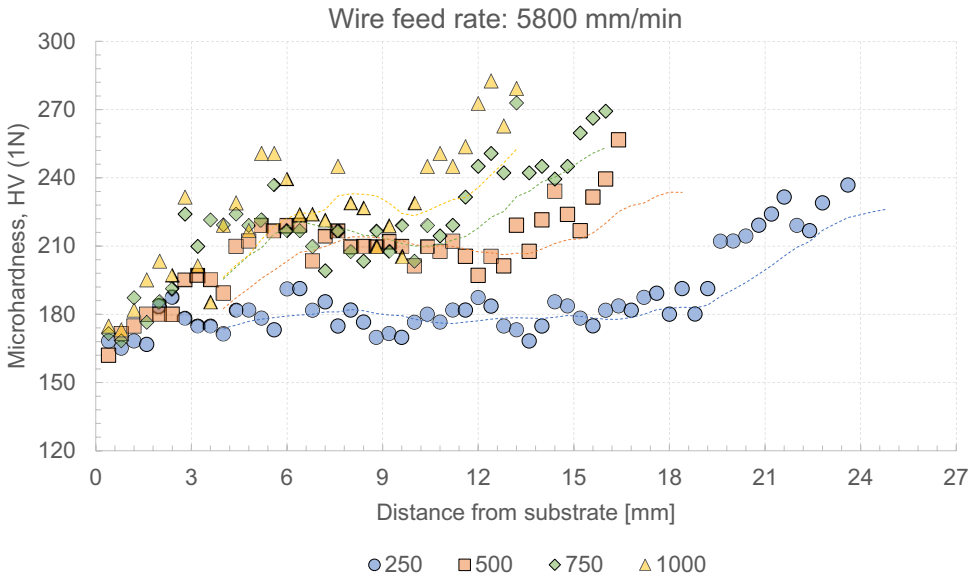


Fig. 19 Microhardness profiles for samples produced with different travel speeds at 5800 mm/min wire feed rate

microstructures in smaller components, such approaches become less practical for very large WAAM structures due to size limitations of heat treatment equipment and thermal mass considerations.

This study investigated the influence of two critical process parameters—travel speed and wire feed rate—on the geometry, thermal history, and resulting microstructure of WAAM components. The geometric analysis revealed that both parameters significantly affect bead dimensions, contradicting previous studies [34–38] that suggested minimal influence of wire feed rate. Our results, supported by a mass conservation model that accurately predicted cross-sectional areas, demonstrate that bead geometry is directly proportional to wire feed rate and inversely proportional to travel speed. This simple yet effective model provides a powerful tool for process planning and parameter selection to achieve desired geometrical characteristics.

The thermal analysis proved essential for understanding the relationship between process parameters and cooling rates, which ultimately determine microstructural evolution and mechanical properties. WAAM components experience complex thermal histories characterized by rapid heating, directional cooling, and multiple thermal cycles during subsequent layer deposition. These thermal conditions vary both with process parameters and spatial location within the build, creating position-dependent microstructures and properties. Higher travel speeds (1000 mm/min) produced cooling rates up to 4 times faster than lower travel speeds (250 mm/min), with significant consequences for microstructural development.

The cooling rates measured in this study align with previous research by Baier et al. [39], who demonstrated that higher interlayer temperatures or shorter dwell times between depositions can contribute to geometrical instability. In our experiments, interlayer temperatures were consistently maintained below 50 °C to minimize such effects. The relationship between cooling rates and mechanical properties corresponds with findings by Ahsan et al. [40], who reported that high heat input deposits (associated with lower travel speeds) exhibit higher ductility, but lower hardness compared to low heat input deposits (higher travel speeds), which demonstrate greater hardness due to increased cooling rates.

The observed microstructural variations within individual samples highlight a critical challenge in WAAM processing: achieving homogeneous material properties throughout the component. Even under identical process conditions, material properties varied significantly from the bottom to the top of each sample. This heterogeneity aligns with observations by Vora et al. [41], who documented similar zonal variations in SS316L WAAM components. The microstructural evolution in our low-carbon steel samples, characterized by ferrite-pearlite structures with varying distributions and morphologies, was strongly influenced by cooling rates. Higher travel speeds produced finer microstructures with more evenly distributed pearlite, consistent with findings by Equbal et al. [42] on the relationship between cooling rates and microstructure in low-carbon steels.

The relationship between grain size and mechanical properties followed the Hall–Petch relationship, with finer grain structures corresponding to higher hardness values. This explains the increased hardness observed in samples produced at higher travel speeds and in the top layers of all samples, where cooling rates were highest. The characteristic "saddle-shaped" hardness distribution observed along the build height reflects the complex interplay between thermal cycling, microstructural evolution, and position-dependent cooling rates.

The present investigation demonstrates how fundamental principles of volume conservation and heat transfer can be applied to understand and predict the influence of key process parameters on WAAM component characteristics. The primary limitations of this study, which should guide future research, include the use of simple wall geometries rather than more complex structures and the restriction of certain process parameters such as voltage and standoff distance. More comprehensive experimental designs incorporating additional variables would provide deeper insights and enhance predictive capabilities.

Future work should focus on developing and validating finite element models that can accurately predict thermal histories, microstructural evolution, and mechanical properties for complex WAAM geometries under varying process conditions. Such models would facilitate process optimization without extensive experimental trials, accelerating the industrial adoption of WAAM technology for large-scale component manufacturing.

5 Conclusions

This study investigated the influence of travel speed and wire feed rate on the geometry, thermal history, and microstructural characteristics of multilayer deposits produced by Wire Arc Additive Manufacturing (WAAM). Based on the experimental results and analysis, the following conclusions can be drawn:

Bead geometry: The cross-sectional geometry of deposited beads is significantly influenced by both travel speed and wire feed rate. A predictive model based on volume conservation accurately describes the cross-sectional area as directly proportional to wire feed rate and inversely proportional to travel speed. The aspect ratio (height-to-width) of deposited beads consistently ranged between 24 and 30%, with both dimensions exhibiting logarithmic decay with increasing travel speed.

Thermal history: Cooling rates are strongly affected by both process parameters, with travel speed exerting the more dominant influence. At lower travel speeds (250 mm/min), cooling rates remained relatively constant (~27 °C/s) across subsequent layers. In contrast, higher travel speeds (1000 mm/min) produced significantly higher cooling rates (up to 115 °C/s) that varied with build height. This greater influence of travel speed stems from its simultaneous impact on both interaction time and thermal mass, while wire feed rate primarily affects the latter. Under high travel speed conditions (1000 mm/min), cooling rates were approximately three times higher than those observed at low travel speeds (250 mm/min).

Microstructural evolution: All samples exhibited three distinct microstructural zones: (1) larger ferrite grains near the substrate, (2) equiaxed ferrite grains in the middle region, and (3) finer structures in the top layers. Grain size ranged from 1 to 8 μm and was inversely proportional to cooling rate, with higher travel speeds producing finer microstructures. The microstructure transitioned from predominantly equiaxed grains near the substrate to increasingly columnar grains with increasing build height, reflecting directional heat flow during deposition.

Mechanical properties: Microhardness increased with travel speed, corresponding to the finer grain structures produced under faster cooling conditions. Average hardness values ranged from 237 HV (at 250 mm/min travel speed) to 283 HV (at 1000 mm/min). Hardness distributions along the build height typically exhibited a "saddle-shaped" profile: lower values near the substrate, a plateau in the middle region, and higher values in the top layers, reflecting the complex thermal history experienced at different positions.

Author contributions F.L. and A.P., supervision; F.L., A.P., P. B. Y., F.P., and E. A., conceptualization methodology; F.L., P. B. Y., and E. A., data curation; F.L., P. B. Y., F.P., and E. A., writing — original draft, writing.

Funding Open access funding provided by Università degli Studi dell'Aquila within the CRUI-CARE Agreement. This research was conducted within the project: "OCEANOS—Monitoraggio coltivazioni e zone marine costiere: Tecnologie satellitari di nuova generazione"—ARS01_00536.
MIUR,ARS01_00536

Data availability The data supporting this study's findings are available from the corresponding author, Francesco Lambiase, upon reasonable request.

Declarations

Conflict of interest The authors declare no competing interests.

Open Access This article is licensed under a Creative Commons Attribution 4.0 International License, which permits use, sharing, adaptation, distribution and reproduction in any medium or format, as long as you give appropriate credit to the original author(s) and the source, provide a link to the Creative Commons licence, and indicate if changes were made. The images or other third party material in this article are included in the article's Creative Commons licence, unless indicated otherwise in a credit line to the material. If material is not included in the article's Creative Commons licence and your intended use is not permitted by statutory regulation or exceeds the permitted use, you will need to obtain permission directly from the copyright holder. To view a copy of this licence, visit http://creativecommons.org/licenses/by/4.0/.

References

1. V. J. Kharat, P. Singh, G. Sharath Raju, D. Kumar Yadav, M. Satyanarayana.Gupta, V. Arun, A. Hussein Majeed and N. Singh, 2023, Additive manufacturing (3D printing): a review of materials, methods, applications and challenges, *Materials Today:*

Proceedings, https://doi.org/10.1016/j.matpr.2023.11.033, 2214–7853.
2. L. Zhou, J. Miller, J. Vezza, M. Mayster, M. Raffay, Q. Justice, Z. Al Tamimi, G. Hansotte, L. D. Sunkara and J. Bernat, 2024, Additive manufacturing: a comprehensive review, *Sensors (Basel)*, 24: https://doi.org/10.3390/s24092668, 1424–8220 (Electronic) 1424–8220 (Linking).
3. Lambiase F, Scipioni SI, Paoletti A (2022) Accurate prediction of the bead geometry in wire arc additive manufacturing process. The International Journal of Advanced Manufacturing Technology 119:7629–7639. https://doi.org/10.1007/s00170-021-08588-w
4. Chakraborty D, Tirumala T, Chitral S, Sahoo BN, Kiran DV, Kumar PA (2022) The state of the art for wire arc additive manufacturing process of titanium alloys for aerospace applications. J Mater Eng Perform 31:6149–6182. https://doi.org/10.1007/s11665-022-07128-1
5. A. E. Davis, C. I. Breheny, J. Fellowes, U. Nwankpa, F. Martina, J. Ding, T. Machry and P. B. Prangnell, 2019, Mechanical performance and microstructural characterisation of titanium alloy-alloy composites built by wire-arc additive manufacture, *Materials Science and Engineering: A*, 765: https://doi.org/10.1016/j.msea.2019.138289, 09215093.
6. Chang T, Fang X, Liu G, Zhang H, Huang K (2022) Wire and arc additive manufacturing of dissimilar 2319 and 5B06 aluminum alloys. J Mater Sci Technol 124:65–75. https://doi.org/10.1016/j.jmst.2022.02.024
7. Z. Gao, Y. Li, H. Shi, F. Lyu, X. Li, L. Wang and X. Zhan, 2023, Microstructure characteristics under varying solidification parameters in different zones during CMT arc additive manufacturing process of 2319 aluminum alloy, *Vacuum*, 214: https://doi.org/10.1016/j.vacuum.2023.112177, 0042207X.
8. Z. Al-Nabulsi, J. T. Mottram, M. Gillie, N. Kourra and M. A. Williams, 2021, Mechanical and X ray computed tomography characterisation of a WAAM 3D printed steel plate for structural engineering applications, *Construction and Building Materials*, 274: https://doi.org/10.1016/j.conbuildmat.2020.121700, 09500618.
9. C.R.Cunningham, J.Wang, V.Dhokia, A.Shrokani and S.T.Newman, 2019, Characterization of austenitic 316LSi stainless steel produced by wire arc additive manufacturing with interlayer cooling 20+,
10. Ceritbinmez F, Günen A, Gürol U, Çam G (2023) A comparative study on drillability of Inconel 625 alloy fabricated by wire arc additive manufacturing. J Manuf Process 89:150–169. https://doi.org/10.1016/j.jmapro.2023.01.072
11. Chen Z, Soh GS (2022) Microstructure and mechanical properties of Wire Arc Additive Manufactured (WAAM) Inconel 718 parts via post heat treatments. Materials Today: Proceedings 70:567–573. https://doi.org/10.1016/j.matpr.2022.09.592
12. Chen X, Kong F, Fu Y, Zhao X, Li R, Wang G, Zhang H (2021) A review on wire-arc additive manufacturing: typical defects, detection approaches, and multisensor data fusion-based model. The International Journal of Advanced Manufacturing Technology 117:707–727. https://doi.org/10.1007/s00170-021-07807-8
13. Wu B, Ji X-Y, Zhou J-X, Yang H-Q, Peng D-J, Wang Z-M, Wu Y-J, Yin Y-J (2021) In situ monitoring methods for selective laser melting additive manufacturing process based on images — a review. China Foundry 18:265–285. https://doi.org/10.1007/s41230-021-1111-x
14. Srivastava M, Rathee S, Patel V, Kumar A, Koppad PG (2022) A review of various materials for additive manufacturing: recent trends and processing issues. J Market Res 21:2612–2641. https://doi.org/10.1016/j.jmrt.2022.10.015
15. Wang F, Williams S, Colegrove P, Antonysamy AA (2012) Microstructure and mechanical properties of wire and arc additive manufactured Ti-6Al-4V. Metall and Mater Trans A 44:968–977. https://doi.org/10.1007/s11661-012-1444-6
16. J. Wang, Z. Zhao, P. Bai, R. Zhang, Z. Zhang, L. Wang, W. Du, F. Wang and Z. Huang, 2023, Microstructure and mechanical properties of AZ31 magnesium alloy prepared using wire arc additive manufacturing, *Journal of Alloys and Compounds*, 939: https://doi.org/10.1016/j.jallcom.2022.168665, 09258388.
17. Wang J, Zhu K, Zhang W, Zhu X, Lu X (2023) Microstructural and defect evolution during WAAM resulting in mechanical property differences for AA5356 component. J Market Res 22:982–996. https://doi.org/10.1016/j.jmrt.2022.11.116
18. B. Saleh, R. Fathi, Y. Tian, N. Radhika, J. Jiang and A. Ma, 2023, Fundamentals and advances of wire arc additive manufacturing: materials, process parameters, potential applications, and future trends, *Archives of Civil and Mechanical Engineering*, 23: https://doi.org/10.1007/s43452-023-00633-7, 1644–9665.
19. J. Vora, N. Parikh, R. Chaudhari, V. K. Patel, H. Paramar, D. Y. Pimenov and K. Giasin, 2022, Optimization of bead morphology for GMAW-based wire-arc additive manufacturing of 2.25 Cr-1.0 Mo steel using metal-cored wires, *Applied Sciences*, 12: https://doi.org/10.3390/app12105060, 2076–3417.
20. Han S-W, Yoo H, Shin S, Kim H, Lee G, Jeon J, Han S, Cho J (2023) Parameter optimization of WAAM with pulsed GMAW for manufacturing propeller-shaped blade. Int J Precis Eng Manuf 24:1103–1110. https://doi.org/10.1007/s12541-023-00797-5
21. Pant H, Arora A, Gopakumar GS, Chadha U, Saeidi A, Patterson AE (2023) Applications of wire arc additive manufacturing (WAAM) for aerospace component manufacturing. The International Journal of Advanced Manufacturing Technology 127:4995–5011. https://doi.org/10.1007/s00170-023-11623-7
22. Rahman Md Arifur and S. Jamal, 2024, In situ process monitoring of multi-layer deposition in wire arc additive manufacturing (WAAM) process with acoustic data analysis and machine learning, https://doi.org/10.1007/s00170-024-13641-5,
23. Franke J, Heinrich F, Reisch RT (2024) Vision based process monitoring in wire arc additive manufacturing (WAAM). J Intell Manuf. https://doi.org/10.1007/s10845-023-02287-x
24. A. L. B. Novelino, G. C. d. Carvalho and M. Ziberov, 2022, Influence of WAAM-CMT deposition parameters on wall geometry, *Advances in Industrial and Manufacturing Engineering*, 5: 100105, 2666–9129.
25. Yehorov Y, da Silva LJ, Scotti A (2019) Exploring the use of switchback for mitigating homoepitaxial unidirectional grain growth and porosity in WAAM of aluminium alloys. The International Journal of Advanced Manufacturing Technology 104(1581–1592):0268–3768
26. Dinovitzer M et al (2019) Effect of wire and arc additive manufacturing (WAAM) process parameters on bead geometry and microstructure. Addit Manuf 26:138–146
27. H M, V., et al. (2023). Effects of arc current and travel speed on the processing of stainless steel via wire arc additive manufacturing (WAAM) process. Journal of Adhesion Science and Technology **38**: 1–18.
28. Goett G, Kozakov R, Uhrlandt D, Schoepp H, Sperl A (2013) Emissivity and temperature determination on steel above the melting point. Welding in the World 57(595–602):0043–2288
29. R. M. Kindermann, M. J. Roy, R. Morana and J. A. Francis, 2022, Effects of microstructural heterogeneity and structural defects on the mechanical behaviour of wire + arc additively manufactured Inconel 718 components, *Materials Science and Engineering: A*, 839: https://doi.org/10.1016/j.msea.2022.142826, 09215093.
30. Crimp MA, Vedula KM (1993) The relationship between cooling rate, grain size and the mechanical behavior of B2 FeAl alloys. Mater Sci Eng, A 165:29–34. https://doi.org/10.1016/0921-5093(93)90623-M
31. A. E112–13(2021), 2021, Grain Size Determination,
32. Petch NJ (1953) The cleavage strength of polycrystals. Journal of the Iron and Steel Institute 174:25–28

33. Lambiase F, Yanala PB, Paoletti A (2025) Thermal, microstructural, and mechanical characterization of early-stage deposition in wire arc additive manufacturing. Int J Adv Manuf Technol 138:953–970. https://doi.org/10.1007/s00170-025-15561-4
34. Xu Z-Z, Dong Z-Q, Yu Z-H, Wang W-K, Zhang J-X (2020) Relationships between microhardness, microstructure, and grain orientation in laser-welded joints with different welding speeds for Ti6Al4V titanium alloy. Transactions of Nonferrous Metals Society of China 30:1277–1289. https://doi.org/10.1016/S1003-6326(20)65295-5
35. Williams SW, Martina F, Addison AC, Ding J, Pardal G, Colegrove P (2016) Wire + arc additive manufacturing. Mater Sci Technol 32:641–647. https://doi.org/10.1179/1743284715y.0000000073
36. Ding D, Pan Z, Cuiuri D, Li H (2015) Wire-feed additive manufacturing of metal components: technologies, developments and future interests. The International Journal of Advanced Manufacturing Technology 81:465–481. https://doi.org/10.1007/s00170-015-7077-3
37. A. Ayed, A. Valencia, G. Bras, H. Bernard, P. Michaud, Y. Balcaen and J. Alexis, 2020, Effects of WAAM process parameters on metallurgical and mechanical properties of Ti-6Al-4V deposits, *Advances in Materials, Mechanics and Manufacturing*: 26–35.
38. Martina F, Mehnen J, Williams SW, Colegrove P, Wang F (2012) Investigation of the benefits of plasma deposition for the additive layer manufacture of Ti–6Al–4V. J Mater Process Technol 212:1377–1386. https://doi.org/10.1016/j.jmatprotec.2012.02.002
39. Baier D, Wolf F, Weckenmann T, Lehmann M, Zaeh MF (2022) Thermal process monitoring and control for a near-net-shape Wire and Arc Additive Manufacturing. Prod Eng Res Devel 16:811–822. https://doi.org/10.1007/s11740-022-01138-7
40. Ahsan MRU, Seo G-J, Fan X, Liaw PK, Motaman S, Haase C, Kim DB (2021) Effects of process parameters on bead shape, microstructure, and mechanical properties in wire + arc additive manufacturing of Al0.1CoCrFeNi high-entropy alloy. J Manuf Process 68:1314–1327. https://doi.org/10.1016/j.jmapro.2021.06.047
41. Vora J, Parmar H, Chaudhari R, Khanna S, Doshi M, Patel V (2022) Experimental investigations on mechanical properties of multi-layered structure fabricated by GMAW-based WAAM of SS316L. J Market Res 20:2748–2757. https://doi.org/10.1016/j.jmrt.2022.08.074
42. Md Israr Equbal, Parwez Alam and R. Ohdar, 2016, Effect of cooling rate on the microstructure and mechanical properties of medium carbon steel, https://doi.org/10.5923/j.ijmee.20160502.01,
43. Tang S, Wang G, Zhang H (2019) In situ 3D monitoring and control of geometric signatures in wire and arc additive manufacturing. Surf Topogr Metrol Prop 7:025013. https://doi.org/10.1088/2051-672X/ab1c98

Publisher's Note Springer Nature remains neutral with regard to jurisdictional claims in published maps and institutional affiliations.